



# Effects of the Inclusion of Ce and Ni Species on Ti for Modification of K10-Clay by Sol-Gel and their Use as Catalysts in the Liquid-Phase Esterification Systems

G. Rangel-Porras · A. Quiroga-Almaguer · A. Ramírez-Hernández ·  
B. Bachiller-Baeza · H. Pfeiffer-Perea · P. Rangel-Rivera

Accepted: 20 June 2023 / Published online: 10 July 2023  
© The Author(s), under exclusive licence to The Clay Minerals Society 2023

**Abstract** The modification of montmorillonite with metallic species affects directly its crystalline structure, texture, porosity, and surface. The interaction of the metallic molecules with the clay matrix, derived from the modification pathway and the characteristics of the adsorbate, modifies the physicochemical properties of montmorillonite, enabling the creation of materials with varied characteristics to be used both as catalysts and adsorbents. Small amounts of metallic species can confer various structural and physicochemical characteristics on

the same montmorillonite matrix, depending on the metal incorporated. The objective of the present study was to create an acid-base catalyst based on montmorillonite K10 (K10 Mnt), modified with Ti, Ce, and Ni, for the catalytic esterification of acetic acid and penta-1-ol. K10-Mnt was modified using particles of Ti and of Ti modified with Ce and Ni. The effect of the inclusion of Ti and modified Ti species on the transformation of the physicochemical properties of the K10 Mnt and their contributions to the catalytic esterification syntheses were investigated. Samples were characterized by scanning electron microscopy coupled to an energy-dispersive X-ray spectroscopy system (SEM-EDS), powder X-ray diffraction (XRD), Fourier-transform infrared spectroscopy (FTIR), physisorption of N<sub>2</sub> at 77 K (BET and BJH), and thermogravimetric analysis (TGA-DTGA). Finally, the original and modified K10 Mnt samples were tested for their catalytic esterification of acetic acid and penta-1-ol in the liquid phase.

G. Rangel-Porras (✉) · A. Quiroga-Almaguer ·  
P. Rangel-Rivera (✉)  
Department of Chemistry, Division of Nature and Exact  
Sciences, University of Guanajuato, Noria Alta s/n,  
36050 Guanajuato, Guanajuato, Mexico  
e-mail: gporras@ugto.mx

P. Rangel-Rivera  
e-mail: pedro.rangel.rivera.dr@gmail.com

A. Ramírez-Hernández  
Institute of Applied Chemistry, University of Papaloapan,  
Circuito Central No. 200, Parque Industrial, Tuxtepec,  
68301 Oaxaca, Mexico

B. Bachiller-Baeza  
Group of Heterogeneous Catalysts for Selective Chemical  
Processes, Institute of Catalysis and Petrochemistry, C/  
Marie Curie 2, Cantoblanco, 28049, Madrid, Spain

H. Pfeiffer-Perea  
Department of Low Dimensional Materials, Institute  
of Materials Research, National Autonomous University  
of Mexico, Circuito Exterior s/n, Ciudad Universitaria,  
Coyoacán, 04510 Mexico City, Mexico

**Keywords** Esterification · Montmorillonite K10 ·  
Sol-gel · Titanium · Titanium-cerium · Titanium-  
nickel

## Introduction

Esterification is an important process in the chemical industry as esters are used in perfumes, cosmetics, flavorings, additives, emulsifiers, plasticizers, polymer precursors, intermediates, and agents in fine chemicals

and drugs (Hamerski et al., 2020; Khan et al., 2021). This process is performed typically with the reaction of carboxylic acid and alcohol, homogeneously catalyzed by Brønsted acid centers in strong mineral acids, but this has several operational and environmental drawbacks deriving from the toxic and corrosive environment of acids, as well as the difficulty of separating the products from the homogeneous catalysis system.

Studies, therefore, have been undertaken (Saravanan et al., 2016; Vijayakumar et al., 2012) to change to a non-toxic, non-corrosive, heterogeneous catalytic process in which the catalyst can be recovered easily from the reaction media in an environmentally friendly manner. For this purpose, a wide variety of solid acid catalysts have been used, e.g. graphene (Roy et al., 2021), modified metal oxides (Nsir et al., 2017), zeolites (Alismaeel et al., 2018), membranes (Zhang et al., 2020), and clay minerals (Tekale & Yadav, 2021). The clay minerals, such as Mnt, have been used as catalytic or adsorbent materials either unmodified or as supports for other reactive phases or chemically active centers (Amaya et al., 2021; Barakan & Aghazadeh, 2021; Chmielarz et al., 2018; Kashif et al., 2020; Khalil et al., 2015; Zhang et al., 2021a) because they have a unique combination of physicochemical and structural characteristics (Bahmanpour et al., 2018; Parisi et al., 2019; Wen et al., 2019).

Acidic sites are located at the terminal O-H groups at the edges of the 2:1 Mnt layers and involve Si-O(H<sup>+</sup>), Al-O(H<sup>+</sup>), Fe-O(H<sup>+</sup>), or Mg-O(H<sup>+</sup>). Structural hydroxyls at the interfacial plane between the tetrahedral and octahedral sheets may also act as Brønsted acid sites (Bailey et al., 2015). The water present in the interlayer can be polarized and display significant potential for donating protons. Likewise, the undersaturated Al<sup>3+</sup> at the edges of the octahedral sheets can act as electron acceptor or Lewis acid sites (Huang et al., 2021). This coexistence of two types of acid sites makes Mnt an ideal material for use as a heterogeneous catalyst in esterification and other acid-catalyzed processes. The surface and/or the matrix of Mnt may also be modified to enhance its capability as a catalyst. The fact that charged species can be removed from the interlamellar space means that space is a dynamic system that can be exploited to increase the surface area, change the porosity, and provide new active centers for adsorption and/or catalysis (Wang et al., 2018). A wide variety of inorganic species has been used for the modification/pillaring of Mnt, such as Cr (Georgescu et al., 2018),

Al (Cardona et al., 2021), Ti (Butman et al., 2020), Fe (Khankhasaeva & Badmaeva, 2020), Zr (Rathinam et al., 2021), La (Silva et al., 2021), Ce (Lai et al., 2021), Ni (Asgari et al., 2021), Cu (Yang et al., 2020), and others. Ti species incorporated on the surface or within the interlayer space of the Mnt can lead to greater interlayer spacing, significant thermal and hydrothermal stability, larger pore sizes, larger specific surface area, and greater acidity than found with other modified/pillared materials (Jin et al., 2019; Romero et al., 2006; Zhang et al., 2021b). In the case of Ti-modified Mnt, a variety of other metals can be added to enhance further the catalytic performance. Of particular interest in the present study was the incorporation of Ce and Ni species, which promotes oxidation-reduction catalysis, photocatalysis, and surface acidity (Natsir et al., 2021; Zhong et al., 2015). These species are particularly useful in modulating the relative contributions of Lewis and Brønsted acid centers leading to weak acid behavior that sometimes benefits the various catalytic processes (Bernardon et al., 2020; Zhang et al., 2017).

The present study, therefore, aimed to determine the catalytic capacity of K10 Mnt modified with Ti, combined with the addition of Ce and Ni, toward the esterification of acetic acid and penta-1-ol, and to relate the physicochemical properties to the catalytic performance.

## Materials and Methods

### Ti/K10-Based Catalyst Synthesis

The clay mineral used was the commercially available montmorillonite K10 (Fluka Inc., Munich, Germany), with a chemical composition of SiO<sub>2</sub> (73%), Al<sub>2</sub>O<sub>3</sub> (14%), Fe<sub>2</sub>O<sub>3</sub> (2.6%), CaO (0.3%), MgO (1.1%), Na<sub>2</sub>O (0.6%), and K<sub>2</sub>O (1.9%). The precursor of the Ti source was titanium(IV) isopropoxide (Sigma-Aldrich Inc., St. Louis, Missouri, USA). Cerium(IV) dioxide (CeO<sub>2</sub>, Merck Inc., Darmstadt, Germany) and nickel(II) chloride (NiCl<sub>2</sub>, Analit Inc., Mexico City, Mexico) were used as sources of Ce and Ni, respectively. The K10 was activated initially by an acid treatment: K10 was dispersed using 6 M hydrochloric acid, maintaining a relationship of 8 mg of K10 per 1 mL of hydrochloric solution. After that, the mixture was stirred constantly and vigorously for 24 h at 25°C, recovering the solid by centrifugation (1.88 xg), and washing with deionized water at least three times. Finally, the solid was dried at 70°C for 24 h.

Titanium and titanium combined with Ce and Ni species were obtained using a process similar to sol-gel: The Ti-based particle suspensions were prepared by adding titanium(IV) isopropoxide dropwise to an aqueous solution of 0.1 M HCl and stirring vigorously until a gel was formed that contained metallic species in the form of titanium oxide and titanium oxide with Ce and Ni species that can modify the K10 using the procedure described below.

Once the activated K10 was totally dried, it was modified with the metallic species: Each suspension of Ti, Ce/Ti, and Ni/Ti was sonicated for 1 h. At the same time, K10-activated powder was suspended in water and stirred for 1 h under room conditions. Based on the chemical formula for K10, the Si content was 34 wt.%. Enough of the Ti alkoxide was added to the K10 to obtain a Ti/Si weight ratio of 1.02. In the synthesis of Ti modified by Ce and Ni, the amounts of CeO<sub>2</sub> and NiCl<sub>2</sub> required were deposited in the alkoxide/HCl suspension to obtain weight ratios for Ce/Ti and Ni/Ti of 0.02 in both cases. Subsequently, each suspension of Ti, Ce/Ti, and Ni/Ti was mixed with the K10-activated suspension with vigorous stirring for 3 h. The resulting materials were separated by centrifugation (1.88 xg) and washed with deionized water at least three times and dried at 70°C for 24 h. Finally, the K10 modified with metallic species were heated at 200°C for 4 h. Four samples were obtained and studied: K10-activated (K10), K10 modified by the inclusion of Ti species (Ti/K10), K10 modified with Ti species and subsequently with Ce (Ce-Ti/K10), and K10 modified with Ti species and subsequently with Ni (Ni-Ti/K10).

### SEM-EDS

The SEM images were collected using a JEOL JSM 6010/LA analytical scanning electron microscope coupled to a Quantax EDS detector device (Bruker Inc., Billerica, Massachusetts, USA). The sample was mounted on an electrically insulating material and then inserted into the high vacuum system before performing the SEM-EDS analysis.

### Powder X-ray Diffraction

An Inel-Equinox diffractometer (Inel Inc., Artenay, France) operated at 25°C, equipped with CuK $\alpha$  radiation (1.54 Å), was used. Samples were prepared as random powders by hand grinding using a mortar and

pestle until a homogeneous sample was obtained. The samples were packed from behind into metal holders with the help of a glass slide, and the entire uncovered surface was exposed to the incident X-rays. The XRD patterns were obtained over the range 2–80°2 $\theta$  at 5°/min scanning velocity, 30 kV voltage, and at a current of 30 mA. Bragg's equation ( $n\lambda = 2d\sin\theta$ ) was used to calculate the interlamellar spaces or *d* spacings.

### FTIR Spectroscopy

The FTIR spectra were collected using a Bruker FTIR Spectrometer Tensor 27 series instrument (Bruker Inc., Markham, Canada). The samples were heated at 80°C for 1 h prior to spectrum acquisition. Using the KBr pellet method, with typical grinding of a mixture of solid and salt in a ratio of 1/100 by weight and pressing, the spectra were acquired in the 4000–400 cm<sup>-1</sup> range.

### Physisorption of N<sub>2</sub> at 77 K

A Micromeritics ASAP-2010 instrument (Micromeritics Inc., Norcross, Georgia, USA) was used for physisorption of N<sub>2</sub>. The BET equation and BJH (Barrett-Joyner-Halenda) method were used to calculate the BET surface area and pore-size distribution, respectively. A vacuum pressure of 500  $\mu$ m Hg at 200°C was applied to all samples, with the aim of eliminating residual N<sub>2</sub> gas molecules from their surfaces and pores.

### TGA-DTA

A Thermal Analyzer SDT-2960 (TA Instruments Inc., New Castle, Delaware, USA) under an airflow with a heating rate of 10°C/min was used.

### Esterification of Acetic Acid and Penta-1-ol

A stirred-batch reflux system equipped with a Dean-Stark trap to collect water was used to carry out the catalytic process. A ratio of 1:1 v/v of penta-1-ol and toluene was placed in a 50 mL round-bottomed flask. After the mixture stabilized on reaching 90°C, a molar ratio of acetic acid containing penta-1-ol of 0.2:1 and 0.1 g/10 mL of the reaction mixture of each catalyst were added to the system under vigorous and

constant stirring. The conversion was quantified by an acid-base volumetric titration technique using 0.1 M normal KOH and phenolphthalein as an indicator (Li et al., 2020; Rangel-Rivera et al., 2018).

## Results

### SEM-EDS

The SEM images (Fig. 1) showed the particle morphologies of each sample. The sample labeled K10 has a flaky morphology. For K10 modified with Ti species (Ti/K10), compact aggregates were seen without significant alteration with respect to the structure of the original clay. In EDS semiquantitative analysis of elements, for K10 modified by Ti with species of Ce and Ni, these metallic materials apparently were dispersed homogeneously on the surface of the clay. Semi-quantitative analysis (Table 1) showed

the variation in the relative percentages of elements depending on the metallic species used as a modifier.

### Powder XRD

The XRD patterns contained peaks characteristic of montmorillonite (Fig. 2). For K10, the XRD pattern showed a wide diffraction band between  $3$  and  $8^\circ 2\theta$  with a maximum centered at  $\sim 5.2^\circ 2\theta$ , corresponding to a  $d_{001}$  for K10 of 1.68 nm. When K10 was modified with Ti species, the formation of crystalline phases typical of Ti was not observed. No anatase ( $25.3$ ,  $38$ ,  $47.6$ , and  $54.8^\circ 2\theta$ ) or rutile signals ( $21$ ,  $27$ ,  $32$ , and  $43^\circ 2\theta$ ) were noted. Nevertheless, the range  $2$ – $14^\circ 2\theta$  (Fig. 3) showed a broad peak, associated with a basal or interlamellar space of  $d_{001}$  of ( $4$ – $8^\circ 2\theta$ ,  $2.21$ – $1.10$  nm). A broad peak between  $3.5$  and  $7^\circ 2\theta$  ( $2.52$  and  $1.26$  nm, respectively) was observed for each clay sample. The wide peak was centered at  $\sim 5.5^\circ 2\theta$  ( $1.61$  nm).

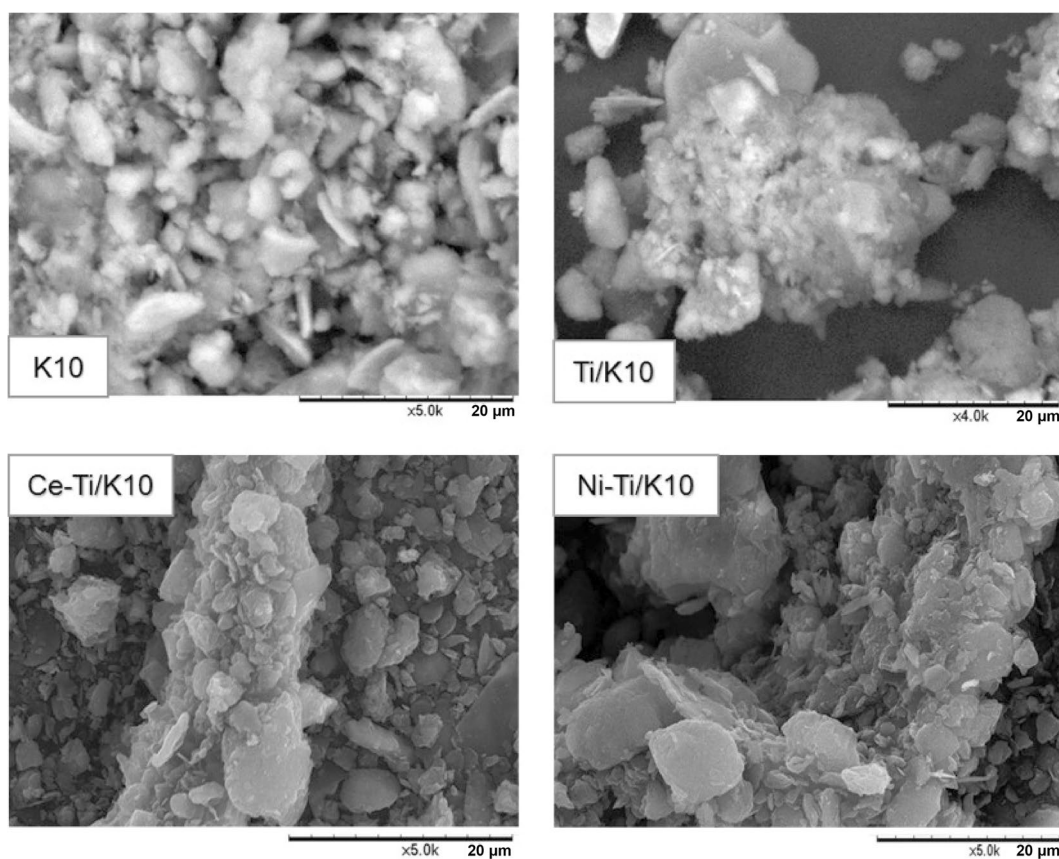


**Fig. 1** SEM images of the clay samples

**Table 1** Semi-quantitative analysis (wt.%) of chemical elements by EDS

Sample/ Element	Si	Al	Fe	K	Mg	Ti	Ce	Ni
K10	69.6	11.4	13.2	3.9	1.9	N.D.	N.D.	N.D.
Ti/K10	66.1	8.7	8.9	2.7	N.D.	13.6	N.D.	N.D.
Ce-Ti/K10	66.9	9.1	8.3	2.0	0.1	13.4	0.2	N.D.
Ni-Ti/K10	67.1	9.8	8.1	0.9	N.D.	13.8	N.D.	0.3

N.D. Not detected by EDS

### FTIR Spectroscopy

The FTIR spectra showed bands typical of montmorillonite (Fig. 4). Peaks between 3700 and 3000  $\text{cm}^{-1}$  were associated with hydroxyl group vibrations and the band at 3620  $\text{cm}^{-1}$  is characteristic of smectites with a large quantity of Al species occupying the octahedral sheets. Likewise, the Si–O stretching vibration modes induce a strong absorption band in the spectral range 1100–1000  $\text{cm}^{-1}$  (Fig. 5). On the other hand, the bands at 525 and 480  $\text{cm}^{-1}$  are

associated with Si–O–Al of octahedral-aluminum ions and Si–O–Si of bending vibrations, respectively, which do not undergo alterations in all cases.

### Physisorption of $\text{N}_2$ at 77 K

Nitrogen adsorption on K10 at 77 K (Fig. 6) showed a well defined type IV isotherm with an inflection point that started at a  $P/P_0$  value of ~0.4; as values approached 1.0, the tendency was for the material to continue adsorbing, as indicated by an asymptotic graph at that

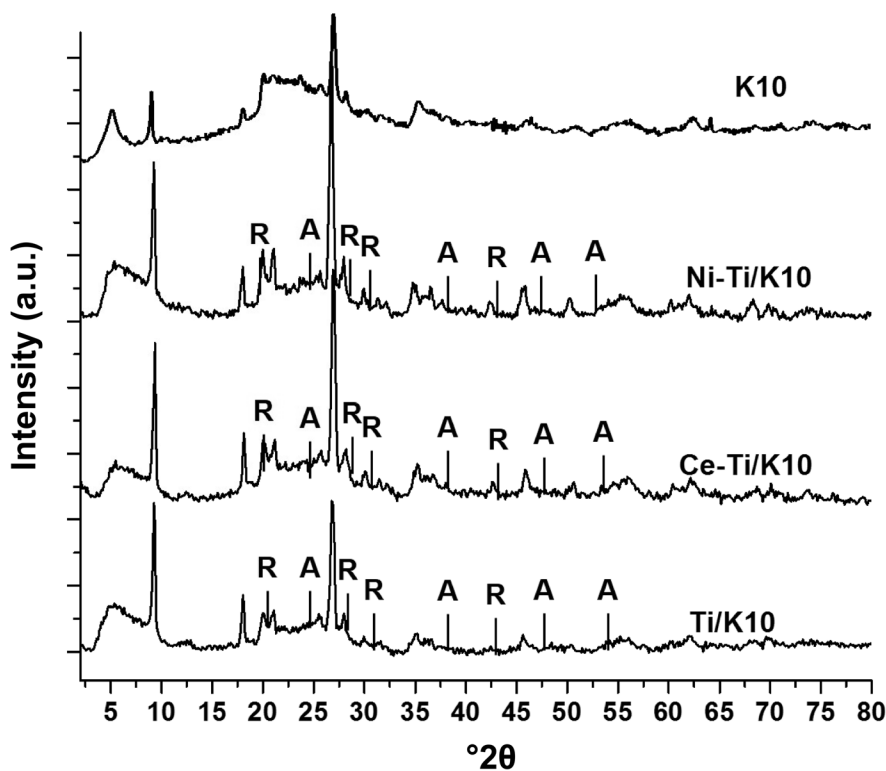


**Fig. 2** Powder XRD of the clay samples. A = anatase ( $\text{TiO}_2$ ), R = rutile ( $\text{TiO}_2$ )



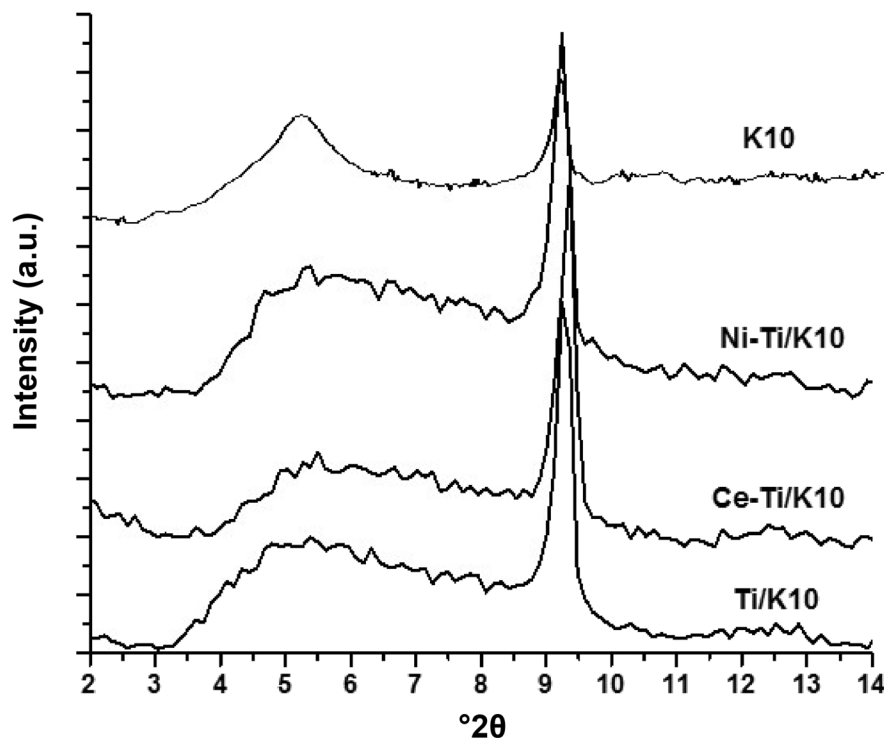


**Fig. 3** Powder XRD of the clay samples in the range 2–14°2 $\theta$

value, suggesting that larger mesopores may accompany slit-shaped pores. The same characteristics were observed in the isotherms of Ti/K10-based samples, and a type H2 (IUPAC) hysteresis-loop was observed in all samples, with some differences in the surface characteristics (Table 2). The BJH adsorption and desorption distribution curves for all samples are shown in Fig. 7; a well-defined peak was observed at 34 Å while a second, less well defined one occurred at 48 Å for K10. The same peaks were present in the curves of Ti/K10-based samples. Note that a second peak was very wide and poorly defined for Ce-Ti/K10 and Ni-Ti/K10, but was better defined in Ti/K10 centered at ~45 Å, due to the morphology of the pores, as well as their dimensions being different both at their entrance and within the matrix.

#### TGA-DTGA

The TGA profiles (Fig. 8) for K10 showed mass losses in several defined stages as the temperature increased: 30–100°C (2.3 wt.%), 100–400°C (1.8 wt.%), and 400–800°C (2.2 wt.%), with a total mass loss of 6.3 wt.%. Mass losses from Ti/K10 for the

same temperature stages were: 30–100°C (2.3 wt.%), 100–400°C (1.8 wt.%), and 400–800°C (1.9 wt.%), for a total weight loss of 6.0%. For Ce-Ti/K10, the weight losses were: 2.9 wt.% at 30–100°C, 3.1 wt.% at 100–400°C, and 2.1% at 400–800°C, resulting in a total weight loss of 8.1%. For Ni-Ti/K10, the values were: 2.4 wt.% (30–100°C), 1.7 wt.% (100–400°C), and 1.8 wt.% (400–800°C), with a total weight loss of 5.9%. The DTGA analysis (Fig. 8) for K10 showed an inflection point at 434°C, while for Ti/K10 the maxima were centered at 425 and 526°C. For Ce-Ti/K10, the corresponding values were 425 and 521°C, and for Ni-Ti/K10 they were 425 and 528°C; the DTGA profiles were very similar to each other in the Ti/K10 samples. All solids with Ti/K10 as the support presented similar weight losses related to endothermic peaks due to the loss of adsorbed water (100–200°C) and dehydroxylation (600–750°C) (Tan, 1998).

#### Esterification of Acetic Acid and Penta-1-ol

The use of clay minerals as heterogeneous catalysts in the esterification of acetic acid and penta-1-ol (Fig. 9)

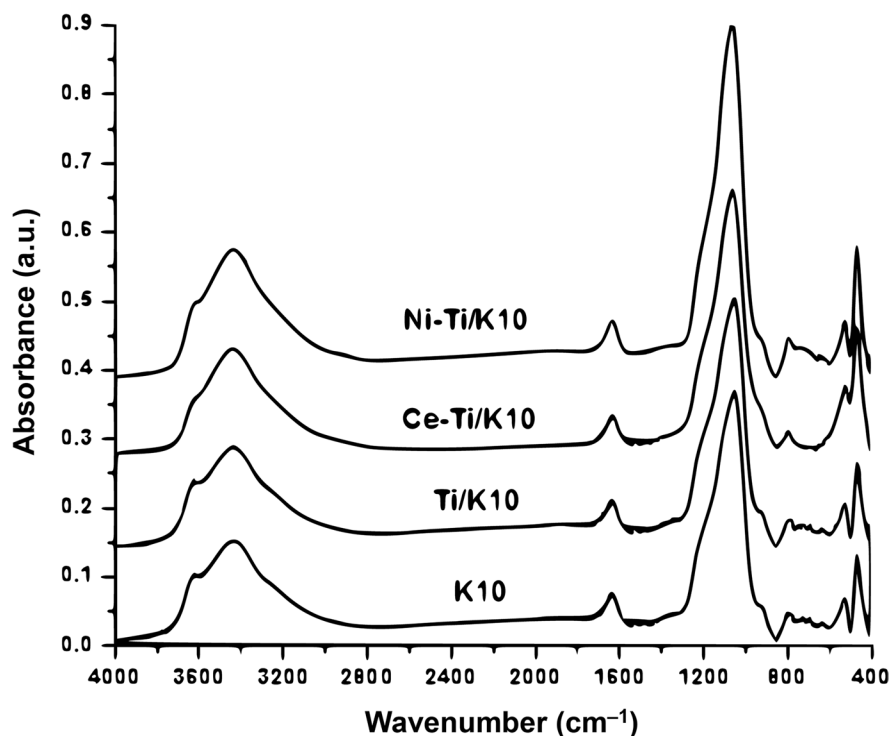


**Fig. 4** FTIR spectra of clay samples

indicated that for K10 the first and second hours of reaction showed little activity; this increased after 3 h until reaching 80% of conversion after 7 h of reaction. During the first hour of reaction, the Ti/K10 catalyst gave 76% conversion; Ce-Ti/K10, 75.0%; and Ni-Ti/K10, 60.0%. After 3 h of reaction, the maximum conversion for both Ti/K10 and Ce-Ti/K10 was 86.0%. For Ni-Ti/K10 the greatest conversion rate, achieved after 8 h of reaction, was 83.0%. The blank experiment (no catalyst) gave ~15.0% of conversion by autocatalytic reaction and the rate of conversion was constant throughout the 8 h of reaction.

## Discussion

### SEM-EDS

The morphology of the K10 sample was flaky in aggregates, a typical and common structure of clays in lamellar arrangements. When K10 was modified with Ti, a heterostructure of the clay was observed, with the appearance of small aggregations on the lamellar surface. The flaky particles of the original K10 changed

to a more spongy morphology as the Ti particles were dispersed on the surface, but without creating a ‘house-of-cards’ type structure; thus the clay layers conglomerated together to create a structure similar to that created by stacking playing cards on top of each other, in the shape of a pyramid. In the Ce-Ti- and Ni-Ti-modified K10 samples, the same behavior as for Ti/K10 was observed, but a more organized structure was noted than for with Ti/K10, i.e. a loose flaky aggregate but without forming a ‘house-of-cards’ structure, in agreement with results described by Belver et al. (2015). The EDS spectroscopy data indicated that the incorporation of Ti species was homogeneous, as well as the detection of other elements, especially in the decrease of percentage of Al and Fe. The homogeneous distribution of the Ti, Ce-Ti, and Ni-Ti species on the surface of the K10 layers was confirmed by these data.

### Powder XRD

The XRD pattern of K10 showed a well defined peak associated with the  $d_{001}$  basal spacing, indicating the swelling of the lamellar structure after the HCl acid treatment, with the subsequent increase in the basal spacing

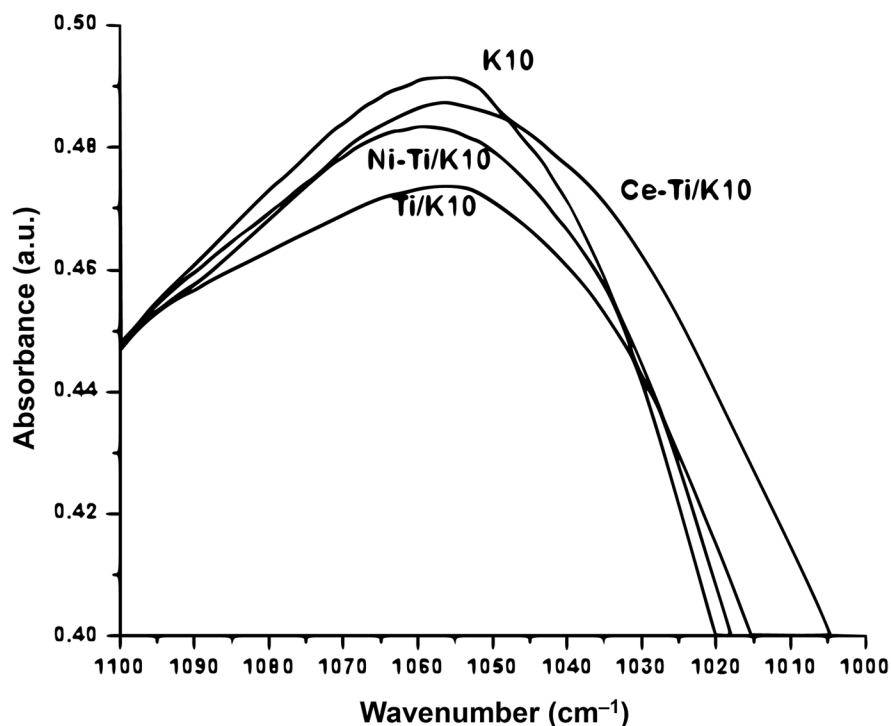


**Fig. 5** FTIR spectra of the clay samples in the range 1100–1000  $\text{cm}^{-1}$

into flakes dispersed heterogeneously (Rangel-Porras et al., 2014; Rangel-Rivera et al., 2014). The absence of peaks assigned to Ti in the XRD patterns of the Ti/K10-based samples indicated a very small amount of Ti, or the presence of non-crystalline Ti particles, or even the absence of Ti particles; the same effect was observed during modification by Ce-Ti and Ni-Ti species. In previous reports (Rangel-Rivera et al., 2014) the K10-activated clay showed a broad peak centered at  $4.9^\circ 2\theta$  (1.8 nm), which is similar to the broad peak observed in the present study at  $\sim 5.5^\circ 2\theta$  (1.61 nm), both of which indicate layer stacking disorder. These interlamellar spaces are greater than those reported in the literature for  $\text{TiO}_2$ -pillared montmorillonites (Binitha & Sugunan, 2006; Liu et al., 2009), leading to the conclusion that the clay minerals studied were not pillared by Ti species, but were only surface modified by Ti, Ce-Ti, and Ni-Ti species, even delaminating K10 to a certain degree.

#### FTIR Spectroscopy

Focusing on the  $-\text{OH}$  stretching region of Ti/K10, the band with a maximum at  $3430 \text{ cm}^{-1}$  corresponds to water molecules fixed to the surface by hydrogen

bonds, resulting in overlapping symmetric-asymmetric stretching vibrations. The peak at  $3615 \text{ cm}^{-1}$  was associated with the structural hydroxyl groups of K10, which suggested that the inclusion of Ni-Ti and Ce-Ti in K10 modified the chemical environment of the hydroxyl groups in the K10 structure into a more homogeneously process than Ti species alone. The shape of the Si–O band is an indicator of montmorillonite intercalation (Cole, 2008; Maier et al., 2021); nevertheless, no variation was observed in the region between 900 and  $850 \text{ cm}^{-1}$ , indicating a similar chemical structure of the cations between samples. A slight change in shape, more defined and elongated, was noted in the Ni-Ti/K10 sample but not in the others, indicating that the interlayer space environment may have been altered. The unmodified bands, thus, at 1090, 525, and  $480 \text{ cm}^{-1}$  suggested that the incorporation of inorganic species in K10 does not modify substantially either the structure or the chemical environment of the interlamellar space, but the modification affects the surface of the material. These data corroborate the information obtained by SEM and XRD, thus reaffirming the hypothesis of modification by



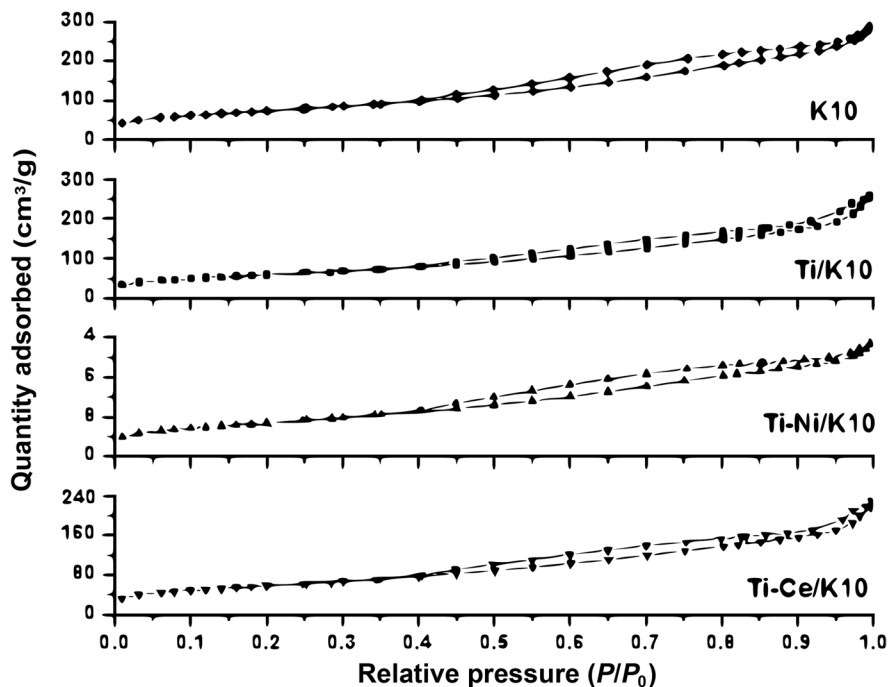


**Fig. 6** N<sub>2</sub> adsorption-desorption isotherms at 77 K for the clay samples

dispersion-deposition but not by pillar or by the formation of a ‘house-of-cards’ structure.

#### Physisorption of N<sub>2</sub> at 77 K

A type IV curve is common in layered materials with the presence of mesopores and explains the tendency to follow the adsorption process at relative pressures ( $P/P_0$ ) > 1.0, relating to pore expansion (Gregg & Sing, 1995). Desorption hysteresis is an indicator of the shape of the pores and their capillary adsorption, indicating that this material with mesopores and H<sub>2</sub> hysteresis is related to solids containing aggregates of particles in the form of parallel plates, with straight, cylindrical pores, which gives rise to pores in the form of slits, although in this case it is the greater heterogeneity of the pores that made up these clays. Furthermore, the presence of micropores was possible due to low adsorption at low relative pressures ( $P/P_0 < 0.03$ ). In the BJH patterns, K10 showed the typical pore distribution of a layered material, and the trend was similar for all the Ti/K10-based samples that were analyzed, which indicated that the shape of the aggregates was practically identical among them. Following Xia and collaborators, the mesopores located at 30 Å

correspond to pores inside the internal layers of the clay, and the pores >40 Å are assigned to mesopores outside the internal layers (Xia et al., 2009). The BJH pattern of K10 showed an incipient peak at 44 Å, which was undetectable in Ti/K10 samples. Deposition of the Ce and Ni species did not alter the structure or geometry of the pores of the original material. Ti/K10, as well as the formation of Ti species on the K10 surface, induced the presence of mesopores exclusively in internal layers of the structure. The differences in desorption hysteresis indicated the formation of these mesopores, where the presence of micropores made only a moderate contribution to the surface area. This type of architectural arrangement at the nanoscale is

**Table 2** Surface area and porosity of clay samples

Sample	BET surface area (m <sup>2</sup> /g)	Pore volume (cm <sup>3</sup> /g)	Pore size (Å)
K10	240	0.31	57.2
Ti/K10	213	0.37	69.2
Ce-Ti/K10	240	0.26	42.7
Ni-Ti/K10	98	0.27	28.7

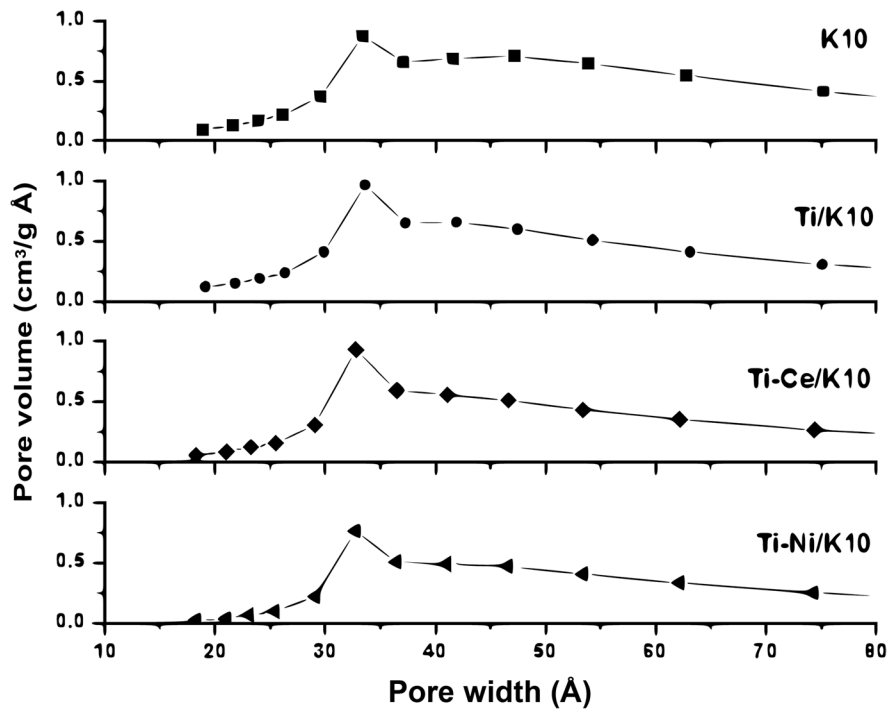


**Fig. 7** BJH pore-size distribution of clay samples

typical of exfoliated specimens or specimens in which the layers are disordered, losing their characteristic interlayer space while the metallic particles adhere to the surfaces of the lamellae (Serwicka, 2021). The incorporation of Ti species does not produce pillaring or delamination of the K10; likewise, modification with

Ce or Ni species does not produce these effects. In the present case, the incorporation of Ni and Ce species in the modified K10 with Ti prompted a decrease in pore size and BET surface area, as some Ce-Ti and Ni-Ti particles remained on the surfaces and edges of the layers. The greater increase in BET surface area of the

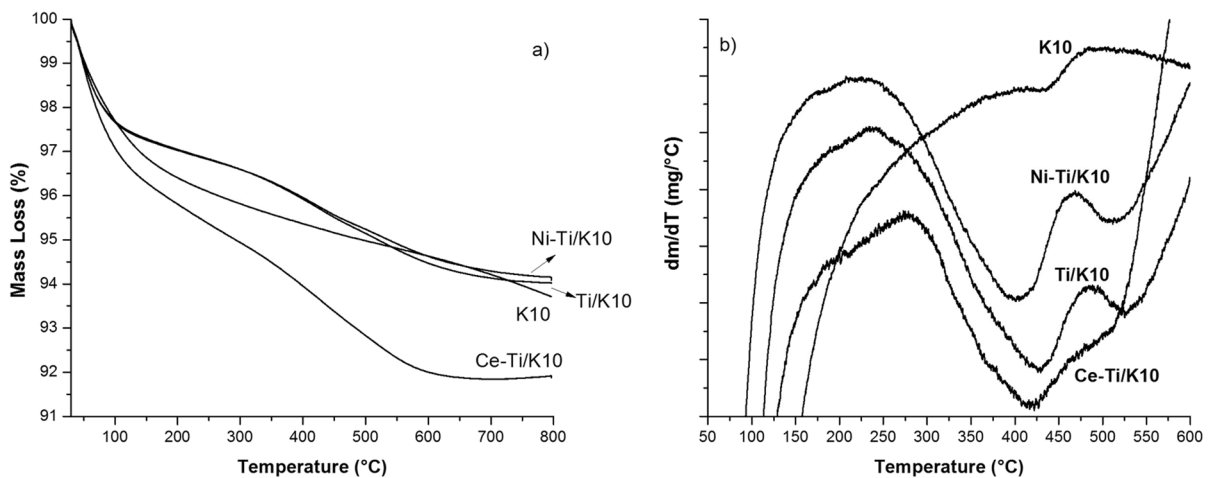


**Fig. 8** a TGA and b DTGA analyses of the clay samples

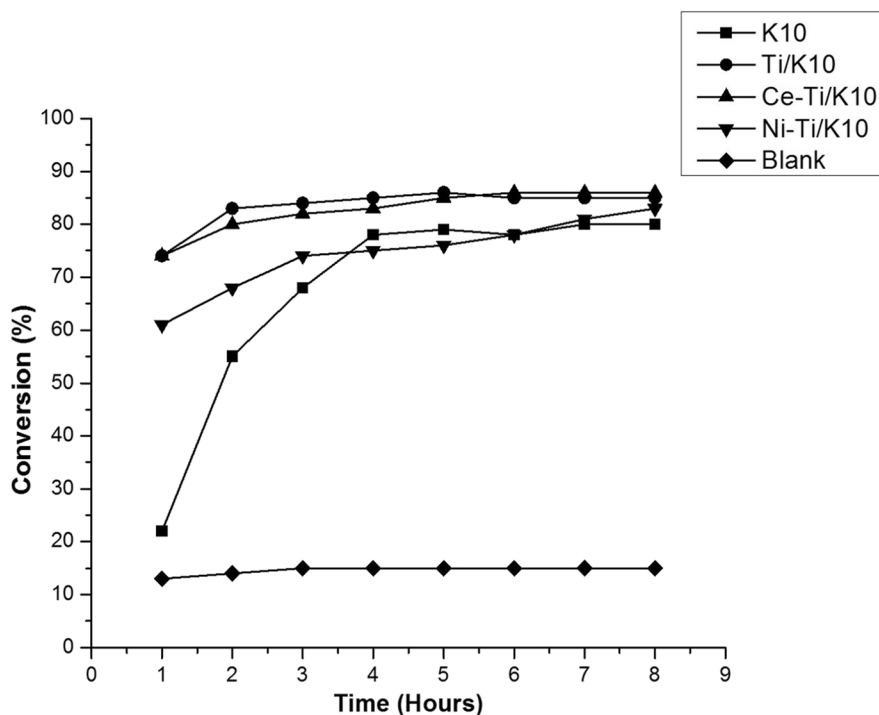


**Fig. 9** Conversion of acetic acid and penta-1-ol during the esterification reaction using the clay samples

Ce-Ti/K10 than that of Ti/K10 is an effect of the crystal sizes of the Ti species tending to shrink in the presence of Ce species, so the BET surface area increased. On the other hand, the presence of Ni species modified the pathways of incorporation of Ti species on the K10 matrix, occupying a minor BET surface area. Finally, two pathways of incorporation are proposed here: (1) the dispersion of species of Ti, Ce-Ti, and Ni-Ti which form, exclusively, the internal mesoporous structure arrangement; and (2) non-hydrolyzed species forming agglomerates which lead to micropores through the aggregation of metallic nanoparticle-clay layers, blocking the presence of mesopores outside the internal layers. These assertions are supported by SEM, XRD, and FTIR characterizations where the morphology of the materials, the absence of pillaring or ‘house-of-cards’ type structures, and the non-delamination of K10 after the inclusion of metallic species are all noted (Fig. 10).

#### TGA-DTGA

When the samples were heated, the first stage was the elimination of all physically adsorbed water; the second stage, the removal of interlayer water and

initiation of dehydroxylation of the K10. The third weight-loss stage,  $>400^{\circ}\text{C}$ , was due to K10 dehydroxylation but also to the carbonization of the organic compounds from the organic systems of Ti species formed during the intercalation of Ti in the clay by a sol-gel process in all samples (Bineesh et al., 2011), which were the result of the hydrolysis (TiOH), alcoxolation-oxolation (Ti-O-Ti), and ololation (Ti-OH-Ti) processes, respectively. On the other hand, a variety of compounds such as  $\text{Ti}\{\text{OCH}(\text{CH}_3)_2\}_3\text{OH}$ ,  $\text{Ti}\{\text{OCH}(\text{CH}_3)_2\}_2(\text{OH})\text{OH}$ ,  $\text{Ti}\{\text{OCH}(\text{CH}_3)_2\}_2(\text{OH})_2$ , or  $\text{Ti}\{\text{OCH}(\text{CH}_3)_2\}(\text{OH})_3$  are derived from the aforementioned processes and present in the sol-gel matrix [Wright & Sommerdijk, 2001]. One study reported that the latter could include the decomposition of two types of organic compounds, one adsorbed on the surface of Ti/K10 ( $>400^{\circ}\text{C}$ ) and the second intercalated in the interlamellar space ( $>600^{\circ}\text{C}$ ), both remnants of the intercalation process of Ti species via sol-gel (Kaneko et al., 2001). During the present study, however, no evidence of intercalation within the interlamellar space was obtained and, thus, the two types apparently were not present. Nevertheless, when the Ti/K10 was modified by Ce and Ni species, some

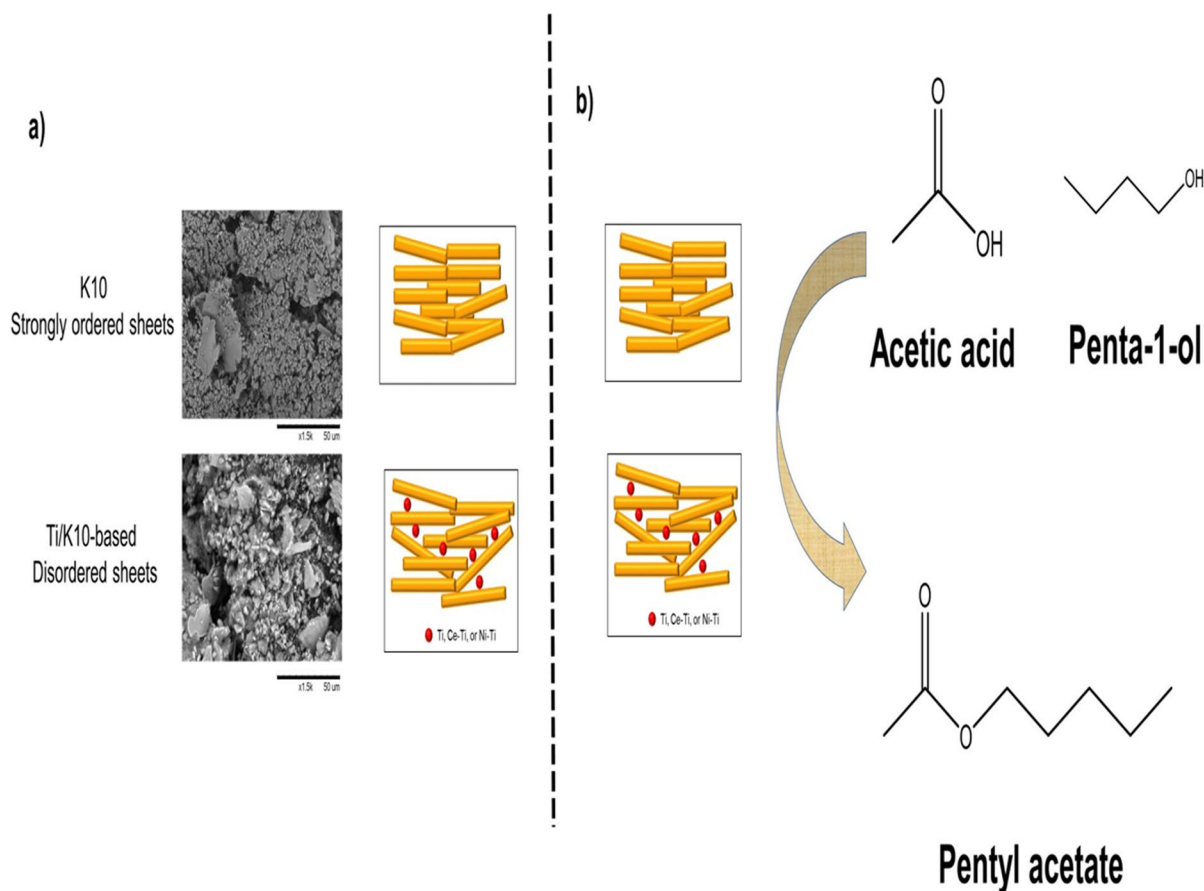


**Fig. 10** a Schematic representation of the structure of the clay samples, b esterification process of the clay samples

slight differences were observed in the TGA profiles of Ti/K10 and Ni-Ti/K10, but Ce-Ti/K10 showed the greatest mass loss of all Ti/K10-based samples.

Due to Ce-Ti/K10 having the largest surface area of all samples, the incorporation of Ce into Ti/K10 may have exposed the metal, which could then become hydrated and account for the slight increase in adsorbed water content observed by TGA (Fig. 5).

#### Esterification of Acetic Acid and Penta-1-ol

The catalysis of esterification using K10 and Ti/K10-based catalysts was carried out with the aim of determining the effect of the inclusion of modified Ce and Ni species on Ti-modified K10. The esterification process is known to be a typical condensation reaction that is acid catalyzed. Note that montmorillonite (K10 included) is a system of colloidal particles which are very stable and highly swelling,

leading to its ability to exfoliate into monolayers (Nicolosi et al., 2013). The phenomenon of delamination or exfoliation has attracted research into their use in heterogeneous catalysis (Roth et al. 2020; Shawky et al., 2019; Yi et al., 2021), and has been especially focused in organic synthesis reactions in the liquid phase. The recovery of the catalyst in these cases is relatively simple, either by deposition of the K10 colloids or by mechanical means such as centrifugation (Chellapandi & Madhumitha, 2022). Once the material is washed, settled, and dried, it can be used again, giving rise to an economic and eco-friendly catalyst (Mahanta et al., 2017). The differences in the catalytic activity are due to changes in the total acidity of the K10 and Ti/K10-based catalysts. On the other hand, the esterification reaction is promoted with the presence of a Brønsted acid catalyst, which is responsible for providing protons ( $H^+$ ) to the reaction medium. Protons interact with

**Table 3** Comparison of various catalysts in the synthesis of pentyl acetate

Catalyst	Temperature (°C)	Conversion (%)	Time (h)	Reference
Montmorillonite K10	90	78.0	5	Rangel-Rivera et al. (2018)
Montmorillonite K10 modified with Zr	90	88.0	4	Rangel-Rivera et al. (2018)
Zeolite ZSM-5	130	43.0	4	Gao et al. (2020)
IL/MIL-101(Cr)	80	82.4	1	Hassan et al. (2017)
Zirconium sulfophenyl phosphonate	50	74.0	14	Curini et al. (2000)
Acid modified attapulgite	117	89.67	3	Pushpalettha & Lalithambika (2011)
Cerium polyoxometalate	25	97.0	15	Mirkhani et al. (2004)
Graphite oxide	90	80.0	2	Mirza-Aghayan et al. (2014)
Ti/K10	90	84.0	3	This study
Ce-Ti/K10	90	86.0	3	This study
Ni-Ti/K10	90	83.0	8	This study

one or both reactants, starting with the catalytic process. K10 showed a lower catalytic performance in the first 3 h of the reaction, reaching its maximum after 6 h. Using the Ti/K10 and Ce-Ti/K10 catalysts offered the best performances. This behavior is related to their greater BET surface area and ability to retain water molecules. The water molecules will be able to disperse in a greater proportion, as well as be retained in the metallic centers. This arrangement results in the dissociation of protons on a larger scale. Furthermore, it highlights the behavior of Ni-Ti/K10 which reached its maximum activity 5 h later than the other two catalysts. This phenomenon may be due to the tendency of nickel species to form agglomerates in inorganic matrices (Iwanschitz et al., 2011; Lee & Kim, 2021), which was observed in the decrease of surface characteristics such as BET surface area, pore size, and pore volume. When they are agglomerated after the incorporation process, the Ni particles reduce the textural properties in order of porosity and BET surface area, as well as the number of metallic centers where the Brønsted acid sites are in the Ti/K10 catalyst. The result of this behavior is an active acid material for esterification processes, but with a delayed catalytic activity relative to the other materials used as catalysts (Fig. 9). Finally, K10 required a longer time to obtain appreciable yields because its acid centers are not as strong or as dispersed as those of the modified materials, despite having greater mesoporosity. Comparing K10 and Ti/K10-based materials with other types of heterogeneous and homogeneous catalysts (Table 3) used for

the conversion of pentyl acetate, the Ti/K10-based catalysts, except for Ni-Ti/K10, offer shorter reaction times and lower temperatures than most of the catalysts presented. In addition, the use of this type of catalyst is advantageous in terms of easy separation, environmental compatibility, and practical manipulation of catalytic process parameters.

## Conclusions

The inclusion of Ti, Ce-Ti, and Ni-Ti species on K10 montmorillonite did not affect its crystalline structure inasmuch as the crystalline phases corresponding to the modified metallic species were not present. Nevertheless, the chemical environment of the catalyst changed depending on modifiers, such that Ti/K10 and Ce-Ti/K10 had surface hydration levels greater than that for Ni-Ti/K10, which generated a greater availability of active acid centers. The incorporation of metallic species did not provoke the formation of structures described in the literature such as pillars or the “house-of-cards” structure; nonetheless, the presence of two types of mesopores in K10 was affected by the incorporation of the metallic species, creating only internal mesopores, affecting the bimodal structure in terms of mesoporosity that was perceptible in K10. Specifically, the incorporation of Ce species caused an increase in the surface area, while modification with Ni species had the opposite effect. This behavior led to a greater amount of organic matter and water in Ce-Ti/K10 so that the incorporation of Ti and

Ti modified with Ce species produced a greater dispersion of the reagents and increased the availability/accessibility of active acid centers. Finally, the inclusion of Ce species produced a structure with a larger porosity that induced a larger BET surface area than its counterparts, while the Ni-modified species led to the formation of agglomerated particles that decreased the BET surface area of the original material. These characteristics were decisive in the catalytic activity of the catalysts, such that Ni-Ti/K10 showed the least conversion over the longest reaction time.

**Acknowledgments** This study was supported by the DAIP-Universidad de Guanajuato office. The authors acknowledge Cristina Daniela Moncada-Sánchez of the Laboratory for Research and Characterization of Minerals and Materials of the University of Guanajuato (LICAMM-UG-Mexico) for the support in the SEM-EDS analysis. Likewise, the authors are grateful to CONACYT-Mexico for the fellowships provided to P. Rangel-Rivera and A. Quiroga-Almaguer.

**Author Contributions** P. Rangel-Rivera, G. Rangel-Porras, and B. Bachiller-Baeza contributed to the experimental development, analysis of results, writing, reviewing, and final editing of the manuscript. A. Ramírez Hernández and A. Quiroga-Almaguer contributed to the analysis of results, reviewing, and final editing of the manuscript. H. Pfeiffer-Perea contributed to the experimental development and reviewing of the manuscript.

#### Declarations

**Conflict of Interest** The authors declare no conflicts of interest with respect to this article.

#### References

- Alismaeel, Z. T., Abbas, A. S., Albayati, T. M., & Doyle, A. M. (2018). Biodiesel from batch and continuous oleic acid esterification using zeolite catalysts. *Fuel*, *234*, 170–176.
- Amaya, J., Moreno, S., & Molina, R. (2021). Heteropolyacids supported on clay minerals as bifunctional catalysts for the hydroconversion of decane. *Applied Catalysis B: Environmental*, *297*, 120464.
- Asgari, M., Vitale, G., & Sundararaj, U. (2021). Synthesis and characterization of a novel nickel pillared–clay catalyst: In-situ carbon nanotube–clay hybrid nanofiller from Ni-PILC. *Applied Clay Science*, *205*, 106064.
- Bahmanpour, A. M., Héroguel, F., Baranowski, C. J., Luterbacher, J. S., & Kröcher, O. (2018). Selective synthesis of dimethyl ether on eco-friendly K10 montmorillonite clay. *Applied Catalysis A: General*, *560*, 165–170.
- Bailey, L., Lekkerkerker, H. N. W., & Maitland, G. C. (2015). Smectite clay – Inorganic nanoparticle mixed suspensions: Phase behaviour and rheology. *Soft Matter*, *11*, 222–236.
- Barakan, S., & Aghazadeh, V. (2021). The advantages of clay mineral modification methods for enhancing adsorption efficiency in wastewater treatment: A review. *Environmental Science and Pollution Research*, *28*, 2572–2599.
- Belver, C., Bedia, J., & Rodriguez, J. J. (2015). Titania–clay heterostructures with solar photocatalytic applications. *Applied Catalysis B: Environmental*, *176*, 278–287.
- Bernardon, C., Osman, M. B., Laugel, G., Louis, B., & Pale, P. (2020). Acidity versus metal-induced Lewis acidity in zeolites for Friedel–Crafts acylation. *Comptes Rendus Chimie*, *20*, 20–29.
- Bineesh, K. V., Kim, D. Y., Kim, M. I., & Park, D. W. (2011). Selective catalytic oxidation of H<sub>2</sub>S over V<sub>2</sub>O<sub>5</sub> supported on TiO<sub>2</sub>-pillared clay catalysts in the presence of water and ammonia. *Applied Clay Science*, *53*, 204–211.
- Binitha, N. N., & Sugunan, S. (2006). Preparation, characterization and catalytic activity of titania pillared montmorillonite clays. *Microporous and Mesoporous Materials*, *93*, 82–89.
- Butman, M. F., Gushchin, A. A., Ovchinnikov, N. L., Gusev, G. I., Zinenko, N. V., Karamysheva, S. P., & Krämer, K. W. (2020). Synergistic effect of dielectric barrier discharge plasma and TiO<sub>2</sub>-pillared montmorillonite on the degradation of rhodamine B in an aqueous solution. *Catalysts*, *10*, 359–376.
- Cardona, Y., Korili, S. A., & Gil, A. (2021). A nonconventional aluminum source in the production of alumina-pillared clays for the removal of organic pollutants by adsorption. *Chemical Engineering Journal*, *425*, 130708.
- Chellapandi, T., & Madhumitha, G. (2022). Montmorillonite clay-based heterogeneous catalyst for the synthesis of nitrogen heterocycle organic moieties: A review. *Molecular Diversity*, *26*, 2311–2339.
- Chmielarz, L., Kowalczyk, A., Skoczek, M., Rutkowska, M., Gil, B., Natkański, P., Radko, M., Motak, M., Dębek, R., & Ryzkowski, J. (2018). Porous clay heterostructures intercalated with multicomponent pillars as catalysts for dehydration of alcohols. *Applied Clay Science*, *160*, 116–125.
- Cole, K. C. (2008). Use of infrared spectroscopy to characterize clay intercalation and exfoliation in polymer nanocomposites. *Macromolecules*, *41*, 834–843.
- Curini, M., Epifano, F., Marcotullio, M. C., Rosati, O., & Rossi, M. (2000). Heterogeneous catalysis in acetylation of alcohols and phenols promoted by zirconium sulfophenyl phosphonate. *Synthetic Communications*, *30*, 1319–1329.
- Gao, X., Ding, Q., Wu, Y., Jiao, Y., Zhang, J., Li, X., & Li, H. (2020). Kinetic study of esterification over structured ZSM-5-coated catalysts based on fluid flow situations in macrocellular foam materials. *Reaction Chemistry & Engineering*, *5*, 485–494.
- Georgescu, A. M., Nardou, F., Zichil, V., & Nistor, I. D. (2018). Adsorption of lead(II) ions from aqueous solutions onto Cr-pillared clays. *Applied Clay Science*, *152*, 44–50.
- Gregg, S. K., & Sing, K. S. (1995). *Adsorption surface area and porosity* (2nd ed.). Academic Press Inc..
- Hamerski, F., Dusi, F. G., Fernandes Dos Santos, J. T., da Silva, V. R., Pedersen Voll, F. A., & Corazza, M. L. (2020). Esterification reaction kinetics of acetic acid and



- n-pentanol catalyzed by sulfated zirconia. *International Journal of Chemical Kinetics*, 52, 499–512.
- Hassan, H. M. A., Betiha, M. A., Mohamed, S. K., El-Sharkawy, E. A., & Ahmed, E. A. (2017). Stable and recyclable MIL-101(Cr)-ionic liquid based hybrid nanomaterials as heterogeneous catalyst. *Journal of Molecular Liquids*, 236, 385–394.
- Huang, W. J., Liu, J. H., She, Q. M., Zhong, J. Q., Christidis, G. E., & Zhou, C. H. (2021). Recent advances in engineering montmorillonite into catalysts and related catalysis. *Catalysis Reviews*, 63, 1–57.
- Iwanschitz, B., Holzer, L., Mai, A., & Schütze, M. (2011). Nickel agglomeration in solid oxide fuel cells: The influence of temperature. *Solid State Ionics*, 211, 69–73.
- Jin, J., Chen, B., Liu, L., Liu, R., Qian, G., Wei, H., & Zheng, J. (2019). A study on modified bitumen with metal doped nano-TiO<sub>2</sub> pillared montmorillonite. *Materials*, 12, 1910–1923.
- Kaneko, T., Shimotsuna, H., Kajikawa, M., Hatamachi, T., Kodama, T., & Kitayama, Y. (2001). Synthesis and photocatalytic activity of titania pillared clays. *Journal of Porous Materials*, 8, 295–301.
- Kashif, M., Halepoto, A., Memon, A., Su, Y., Abdullaha, M., & Soomro, M. Y. (2020). Gallium oxide impregnated on porous clay heterostructures material for selective catalytic reduction of nitrogen oxide with C<sub>3</sub>H<sub>6</sub>. *Journal of Environmental Chemical Engineering*, 8, 103943.
- Khalil, T. A., Chaabene, S. B., Boujday, S., Blanchard, J., & Bergaoui, L. (2015). A new method for elaborating mesoporous SiO<sub>2</sub>/montmorillonite composite materials. *Journal of Sol-Gel Science and Technology*, 75, 436–446.
- Khan, Z., Javed, F., Shamair, Z., Hafeez, A., Fazal, T., Aslam, A., Zimmerman, W. B., & Rehman, F. (2021). Current developments in esterification reaction: A review on process and parameters. *Journal of Industrial and Engineering Chemistry*, 103, 80–101.
- Khankhasaeva, S. T., & Badmaeva, S. V. (2020). Removal of p-aminobenzene sulfanilamide from water solutions by catalytic photo-oxidation over Fe-pillared clay. *Water Research*, 185, 116212.
- Lai, F., Yan, F., Wang, P., Qu, F., Shen, X., & Zhang, Z. (2021). Efficient one-pot synthesis of ethyl levulinate from carbohydrates catalysed by Wells-Dawson heteropolyacid supported on Ce–Si pillared montmorillonite. *Journal of Cleaner Production*, 324, 129276.
- Lee, J. R., & Kim, Y. H. (2021). Agglomeration of nickel oxide particle during hydrogen reduction at high temperature in a fluidized bed reactor. *Chemical Engineering Research and Design*, 168, 193–201.
- Li, L., Yan, B., Li, H., Yu, S., & Ge, X. (2020). Decreasing the acid value of pyrolysis oil via esterification using ZrO<sub>2</sub>/SBA-15 as a solid acid catalyst. *Renewable Energy*, 146, 643–650.
- Liu, J., Dong, M., Zuo, S., & Yu, Y. (2009). Solvothermal preparation of TiO<sub>2</sub>/montmorillonite and photocatalytic activity. *Applied Clay Science*, 43, 156–159.
- Mahanta, A., Raul, P. K., Saikia, S., Bora, U., & Thakur, A. J. (2017). Methanol aided synthesis of PdNPs decorated on montmorillonite K 10 and its implication in Suzuki Miyaura type cross coupling reaction under base free condition. *Applied Organometallic Chemistry*, 32, e4192.
- Maier, M., Beuntner, N., & Thienel, K. C. (2021). Mineralogical characterization and reactivity test of common clays suitable as supplementary cementitious material. *Applied Clay Science*, 202, 105990.
- Mirkhani, V., Tangestaninejad, S., Moghadam, M., Yadollahi, B., & Alipanah, L. (2004). Cerium polyoxometalate as a reusable catalyst for acetylation and formylation of alcohols. *Chemical Monthly*, 135, 1257–1263.
- Mirza-Aghayan, M., Boukherroub, R., & Rahimifard, M. (2014). Graphite oxide as an efficient solid reagent for esterification reactions. *Turkish Journal of Chemistry*, 38, 859–864.
- Natsir, M., Putri, Y. I., Wibowo, D., Maulidiyah, M., Salim, L. O. A., Azis, T., Bijang, C. M., Mustapa, F., Irwan, I., Arham, Z., & Nurdin, M. (2021). Effects of Ni–TiO<sub>2</sub> pillared clay–montmorillonite composites for photocatalytic enhancement against reactive orange under visible light. *Journal of Inorganic and Organometallic Polymers and Materials*, 31, 3378–3388.
- Nicolosi, V., Chhowalla, M., Kanatzidis, M. G., Strano, M. S., & Coleman, J. N. (2013). Liquid exfoliation of layered materials. *Science*, 340(6139), 1226419–1226419.
- Nsir, S. B., Younes, M. K., Rives, A., & Ghorbel, A. (2017). Characterization and reactivity of zirconia-doped phosphate ion catalyst prepared by sol–gel route and mechanistic study of acetic acid esterification by ethanol. *Journal of Sol-Gel Science and Technology*, 84, 349–360.
- Parisi, F., Lazzara, G., Merli, M., Milioto, S., Princivalle, F., & Sciascia, L. (2019). Simultaneous removal and recovery of metal ions and dyes from wastewater through montmorillonite clay mineral. *Nanomaterials*, 9, 1699–1714.
- Pushpaletta, P., & Lalithambika, M. (2011). Modified attapulgite: An efficient solid acid catalyst for acetylation of alcohols using acetic acid. *Applied Clay Science*, 51, 424–430.
- Rangel-Porras, G., Rangel-Rivera, P., Pfeiffer-Perea, H., & Gonzalez-Muñoz, P. (2014). Changes in the characteristics of acid-treated clay after the inclusion of proteins. *Surface and Interface Analysis*, 47, 135–141.
- Rangel-Rivera, P., Rangel-Porras, G., Pfeiffer-Perea, H., & Lima-Muñoz, E. (2014). Thermoanalytical study of acid-treated clay containing amino acid immobilized on its surface. *Journal of Thermal Analysis and Calorimetry*, 115, 1359–1369.
- Rangel-Rivera, P., Bachiller-Baeza, M. B., Galindo-Esquivel, I., & Rangel-Porras, G. (2018). Inclusion of Ti and Zr species on clay surfaces and their effect on the interaction with organic molecules. *Applied Surface Science*, 445, 229–241.
- Rathinam, K., Atchudan, R., & Edison, T. N. J. I. (2021). Zirconium oxide intercalated sodium montmorillonite scaffold as an effective adsorbent for the elimination of phosphate and hexavalent chromium ions. *Journal of Environmental Chemical Engineering*, 9, 106053.
- Romero, A., Dorado, F., Ascencio, I., García, P. B., & Valverde, J. L. (2006). Ti-pillared clays: Synthesis and general characterization. *Clays and Clay Minerals*, 54, 737–747.
- Roth, W. J., Sasaki, T., Wolski, K., Song, Y., Tang, D.-M., Ebina, Y., Ma, R., Grzybek, J., Kałahurska, K., Gil, B., Mazur, M., Zapotoczny, S., & Cejka, J. (2020).

- Liquid dispersions of zeolite monolayers with high catalytic activity prepared by soft-chemical exfoliation. *Science Advances*, 6, 1–6.
- Roy, A. S., Poulouse, A. C., Bakandritsos, A., Varma, R. S., & Otyepka, M. (2021). 2D graphene derivatives as heterogeneous catalysts to produce biofuels via esterification and trans-esterification reactions. *Applied Materials Today*, 23, 101053.
- Saravanan, K., Tyagi, B., & Bajaj, H. C. (2016). Esterification of stearic acid with methanol over mesoporous ordered sulfated ZrO<sub>2</sub>-SiO<sub>2</sub> mixed oxide aerogel catalyst. *Journal of Porous Materials*, 23, 937–946.
- Serwicka, E. W. (2021). Titania-clay mineral composites for environmental catalysis and photocatalysis. *Catalysts*, 11, 1087–1159.
- Shawky, A., El-Sheikh, S. M., Rashed, M. N., Abdo, S. M., & El-Dosoqy, T. I. (2019). Exfoliated kaolinite nanolayers as an alternative photocatalyst with superb activity. *Journal of Environmental Chemical Engineering*, 7, 103174.
- Silva, J. B., Cabral, G. G., Araujo, M. D. S., Caldeira, V. P. S., Coriolano, A. C. F., Fernandes, V. J., Jr., Pergher, S. B. C., & Araujo, A. S. (2021). Catalytic pyrolysis of atmospheric residue of petroleum using pillared interlayered clay containing lanthanum and aluminum polyhydroxycations (LaAl<sub>13</sub>-PILC). *Petroleum Science and Technology*, 39, 704–717.
- Tan, K. H. (1998). *Principles of soil chemistry* (3rd ed.). CRC Press.
- Tekale, D. P., & Yadav, G. D. (2021). Esterification of propanoic acid with 1,2-propanediol: Catalysis by cesium exchanged heteropoly acid on K-10 clay and kinetic modelling. *Reaction Chemistry & Engineering*, 6, 313–320.
- Vijayakumar, B., Mahadevaiah, N., Nagendrappa, G., & Prakash, B. S. J. (2012). Esterification of stearic acid with p-cresol over modified Indian bentonite clay catalysts. *Journal of Porous Materials*, 19, 201–210.
- Wang, Y., Zheng, Z., Zhao, Y., Huang, J., Zhang, Z., Cao, X., Dai, Y., Hua, R., & Liu, Y. (2018). Adsorption of U(VI) on montmorillonite pillared with hydroxyaluminum. *Journal of Radioanalytical and Nuclear Chemistry*, 317, 69–80.
- Wen, K., Zhu, J., Chen, H., Ma, L., Liu, H., Zhu, R., Xi, Y., & He, H. (2019). Arrangement models of Keggin-Al<sub>30</sub> and Keggin-Al<sub>13</sub> in the interlayer of montmorillonite and the impacts of pillaring on surface acidity: A comparative study on catalytic oxidation of toluene. *Langmuir*, 35, 382–390.
- Wright, J. D., & Sommerdijk, N. A. J. M. (2001). *Sol-gel materials chemistry and applications*. CRC Press Taylor & Francis Group.
- Xia, M., Jian, Y., Li, F., Sun, M., Xue, B., & Chen, X. (2009). Preparation and characterization of bimodal mesoporous montmorillonite by using single template. *Colloids and Surfaces A*, 338, 1–6.
- Yang, F., Spyrou, K., Thomou, E., Kumar, S., Cao, H., Stuart, M. C. A., Pei, Y., Gournis, D., & Rudolf, P. (2020). Smectite clay pillared with copper complexed polyhedral oligosilsesquioxane for adsorption of chloridazon and its metabolites. *Environmental Science: Nano*, 7, 424–436.
- Yi, H., Zhao, Y., & Song, S. (2021). Development of superior stable two-dimensional montmorillonite nanosheet based working nanofluids for direct solar energy harvesting and utilization. *Applied Clay Science*, 200, 105886.
- Zhang, L., Qin, Y., Ji, D., Chu, G., Gao, X., Zhang, X., & Song, S. (2017). Effect of cerium ions initial distribution on the crystalline structure and catalytic performance of CeY zeolite. *Journal of Rare Earths*, 35, 791–799.
- Zhang, J., Li, X., He, B., Song, Y., Ji, Y., Cui, Z., Li, J., & Younas, M. (2020). Biodiesel production through heterogeneous catalysis using a novel poly(phenylene sulfide) catalytic membrane. *Energy & Fuels*, 34, 7422–7429.
- Zhang, T., Wang, W., Zhao, Y., Bai, H., Wen, T., Kang, S., Song, G., Song, S., & Komarneni, S. (2021a). Removal of heavy metals and dyes by clay-based adsorbents: From natural clays to 1D and 2D nano-composites. *Chemical Engineering Journal*, 420, 127574.
- Zhang, Q., Zhang, Y., Liu, S., Wu, Y., Zhou, Q., Zhang, Y., Zheng, X., Han, Y., Xie, C., & Liu, N. (2021b). Adsorption of deoxynivalenol by pillared montmorillonite. *Food Chemistry*, 343, 128391.
- Zhong, L., Cai, W., Yu, Y., & Zhong, Q. (2015). Insights into synergistic effect of chromium oxides and ceria supported on Ti-PILC for NO oxidation and their surface species study. *Applied Surface Science*, 325, 52–63.

Springer Nature or its licensor (e.g. a society or other partner) holds exclusive rights to this article under a publishing agreement with the author(s) or other rightsholder(s); author self-archiving of the accepted manuscript version of this article is solely governed by the terms of such publishing agreement and applicable law.